High dynamic range imaging with a single-mode pupil remapping system: a self-calibration algorithm for redundant interferometric arrays

S. Lacour,[1]⋆ E. Thiébaut[2] and G. Perrin[1]

[1]*Observatoire de Paris – Laboratoire d'Etudes Spatiales et d'Instrumentation en Astrophysique, UMR-8109, 5 place Jules Janssen, F-92195 Meudon, France*
[2]*Centre de Recherches Astronomiques de Lyon, UMR-5574, 9 avenue Charles André, F-69561 Saint Genis Laval Cedex, France*

ABSTRACT

The correction of the influence of phase corrugation in the pupil plane is a fundamental issue in achieving high dynamic range imaging. In this paper, we investigate an instrumental set-up which consists of applying interferometric techniques on a single telescope, by filtering and dividing the pupil with an array of single-mode fibres. We developed a new algorithm, which makes use of the fact that we have a redundant interferometric array, to completely disentangle the astronomical object from the atmospheric perturbations (phase and scintillation). This self-calibrating algorithm can also be applied to any – diluted or not – redundant interferometric set-up. On an 8-m telescope observing at a wavelength of 630 nm, our simulations show that a single-mode pupil remapping system could achieve, at a few resolution elements from the central star, a raw dynamic range up to 10^6, depending on the brightness of the source. The self-calibration algorithm proved to be very efficient, allowing image reconstruction of faint sources (magnitude = 15) even though the signal-to-noise ratios of individual spatial frequencies are of the order of 0.1. We finally note that the instrument could be more sensitive by combining this set-up with an adaptive optics system. The dynamic range would however be limited by the noise of the small, high-frequency displacements of the deformable mirror.

Key words: atmospheric effects – instrumentation: adaptive optics – techniques: high angular resolution – techniques: interferometric – stars: imaging – planetary systems.

1 INTRODUCTION

The image obtained though a telescope is a convolution between the brightness distribution of the astrophysical object and the point spread function (PSF). In the Fourier domain, it is the multiplication of the Fourier transform of the object and the optical transfer function (OTF). To restore a correct image of the source, one therefore needs to know precisely the OTF. In the presence of static aberrations only, deconvolution is possible since the OTF can be obtained by observing an unresolved object. But when the OTF is changing with time – e.g. in the presence of atmospheric turbulence – calibration requires averaging the perturbations, whose parameters vary with time. This is one of the reasons why speckle interferometry (Labeyrie 1970), one of the most well-known post-processing techniques, still has some difficulty in creating high dynamic range maps.

This mainly explains why real-time adaptive optics (AO) systems are a fundamental feature of large telescopes. With such systems, the OTF of the telescope is controlled by the deformable mirror to be the same as that of an uncorrupted telescope. However, technological limits appear for (i) larger telescopes (e.g. extremely large telescopes), (ii) shorter wavelengths (e.g. visible) or (iii) extremely high dynamic range imaging (extreme AO). In these three cases it may be advantageous to contemplate a complementary approach using post-detection techniques. The combination of both could be the solution to reach major scientific results like extrasolar planetary system imaging. However, to do so, such techniques would require the knowledge of the time varying OTF.

In Perrin et al. (2006), we proposed a passive solution (i.e. requiring no real-time modification of the optical path) by using a remapping of the pupil. Single-mode fibres provide us with the technology allowing such a massive modification of the geometry of the pupil, while keeping zero optical path differences. In addition, they also provide perfect spatial filtering. Data collection and analysis are then similar to

⋆E-mail: sylvestre.lacour@obspm.fr

those utilized for aperture masking (Haniff et al. 1987; Tuthill et al. 2000), with the noticeable advantage of having the flux of the whole entrance pupil, and the possibility to completely disentangle instrumental from astrophysical information.

In Section 2 we explain why imaging through turbulence is an ill-posed problem. After a recall of the principle of the instrument, we show in Section 3 how what was before an ill-posed problem can become a well-posed one. This translates into an algorithm described in Section 3.3. Finally, we show in the simulations of Section 4 that we can therefore reconstruct perfect images with a dynamic range only limited by detector and photon noise. In Section 5 we conclude by giving a brief summary of our results.

2 THE ILL-POSED PROBLEM OF IMAGING THROUGH TURBULENCE

The image formed in the focal plane of a telescope is the convolution of the object brightness distribution $O(x)$ with the point spread function PSF (x) of the instrument:

$$I(x) = O(x) * \text{PSF}(x). \tag{1}$$

In the Fourier domain, the convolution operation is transformed into a multiplication, while the Fourier transform of the PSF is the OTF:

$$\mu(u) = V(u) \times \text{OTF}(u). \tag{2}$$

We choose $\mu(u)$ as the Fourier transform of the image, and $V(u)$ as the Fourier transform of the object brightness distribution. This is to be in line with interferometric conventions, where it is also called the visibility function. The fact that the image depends on two unknown functions, $V(u)$ and $\text{OTF}(u)$, is the problem underlying any image reconstruction algorithm; without adding further information, we have no way to disentangle the object from the PSF.

Following an interferometric approach, we discretize the OTF to reduce the problem to a system of observables and unknowns. The OTF results from the autocorrelation of the complex values of the complex amplitude transmission inside the pupil. Thus, the OTF can be discretized by considering the pupil as being made of a number of coherent patches where phase and amplitude variations are negligible. Each patch is defined by a position vector r_i and a complex amplitude transmission:

$$G(r_i) = g_i \, e^{i\phi_i} \tag{3}$$

with a phase ϕ_i (e.g. atmospheric piston), an amplitude g_i (e.g. scintillation) and where $i^2 \overset{\text{def}}{=} -1$. Each pair of patches (i, j) selects one specific spatial frequency described by the frequency vector $u_k = (r_i - r_j)/\lambda$, where r_i and r_j are the location vectors of the patches projected in a plane perpendicular to the line of sight and λ is the wavelength. Hence, the OTF at frequency vector u_k is obtained by the relation

$$\text{OTF}(u_k) = \sum_{(i,j)\in\mathcal{B}_k} G(r_i)\, G(r_j)^\star, \tag{4}$$

where $\mathcal{B}_k$ is the set of aperture pairs which sample the kth spatial frequency u_k:

$$\mathcal{B}_k = \{(i,\, j) \, : \, (r_i - r_j)/\lambda = u_k\}. \tag{5}$$

This shows that the OTF can be obtained from the knowledge of the complex amplitude transmission inside the pupil. Using equation (2), we can deduce a direct relation between the pupil transmission, the Fourier transform of the image, and the Fourier transform of the brightness distribution of the object:

$$\mu(u_k) = V(u_k) \sum_{(i,j)\in\mathcal{B}_k} G(r_i)\, G(r_j)^\star. \tag{6}$$

Or to simplify the notation:

$$\mu_k = V_k \sum_{(i,j)\in\mathcal{B}_k} G_i\, G_j^\star, \tag{7}$$

where, and hereinafter, we define $\mu_k \overset{\text{def}}{=} \mu(u_k)$, $V_k \overset{\text{def}}{=} V(u_k)$, $\text{OTF}_k \overset{\text{def}}{=} \text{OTF}(u_k)$ and $G_i \overset{\text{def}}{=} G(r_i)$.

The image reconstruction problem is then reduced to finding the unknowns $\{V_k, G_i; \forall k, \forall i\}$ given the μ_k values. The ill-posedness of this task can be exhibited thanks to a simple example. In Fig. 1, the complex amplitude transmission in the pupil is binned into six different elements (the G_i values). The autocorrelation of these six patches creates an OTF defined by a real value OTF_0 (at central spatial frequency) and nine complex values ($\text{OTF}_1, \dots, \text{OTF}_9$). These OTF values multiplied by the visibility function of the astronomical object ($V_0 \equiv 1$, $V_1, \dots, V_9$) yield the Fourier transform of the observed image as one real value μ_0 and nine complex values ($\mu_1, \dots, \mu_9$). Since, by definition, the real value V_0 is equal to 1 and since the phase of one of the complex amplitude transmissions can be arbitrarily chosen, the image reconstruction involves the computation of 29 unknowns (15 complex values: $G_0, \dots, G_5, V_1, \dots, V_9$, minus an arbitrary phase) given only 19 measurements (the real value μ_0 and the nine complex values $\mu_1, \dots, \mu_9$). Our example demonstrates that the image reconstruction when the PSF is unknown is an ill-posed problem termed as *blind deconvolution* (Thiébaut & Conan 1995). Without adding further information, disentangling astronomical from instrumental information is impossible.
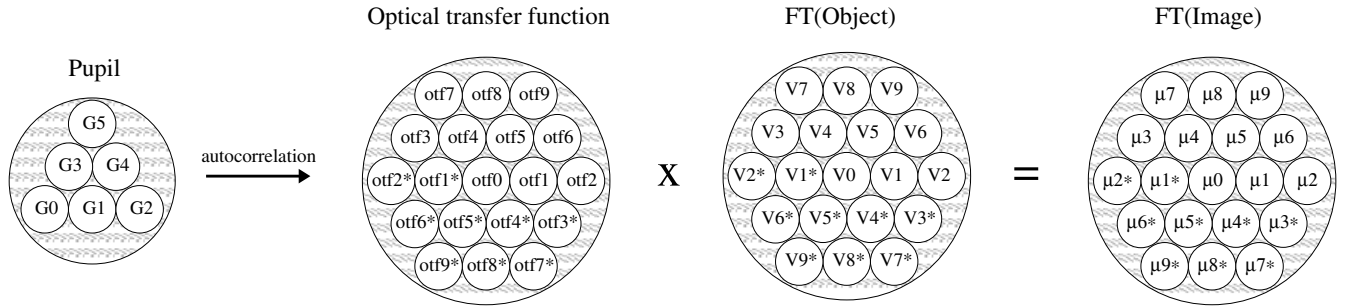
Figure 1. This sketch illustrates equations (4) and (7). The OTF result from the autocorrelation of the pupil complex amplitude transmission, and the Fourier transform of the image is the multiplication of the OTF by the Fourier transform of the object observed. The unknowns are the 15 complex values $\{G_0, \ldots, G_5, V_1, \ldots, V_9\}$, whereas the observables provide only nine complex values $\{\mu_1, \ldots, \mu_9\}$. Deconvolution is therefore an ill-posed problem.

To avoid having to disentangle the time-dependent OTF, a traditional solution is to average its fluctuations. Over multiple observations, the long exposure OTF is

$$\text{OTF}_k = \left\langle \sum_{(i,j)\in\mathcal{B}_k} G_i\, G_j^\star \right\rangle. \tag{8}$$

To calibrate the OTF, the astronomer can observe a point-like star (i.e. such that $V_k = 1, \forall k$) and apply the same averaging process. However, when phase variations become larger than wavelength, the average of the complex OTF tends towards 0, and deconvolution is impossible with a finite signal-to-noise ratio (S/N) (Thiébaut 2005). In practice, long exposure images have a λ/r_0 effective resolution, where $r_0 \simeq 20$ cm in the visible is Fried's parameter. Two solutions have been proposed to overcome this problem and achieve the diffraction limit at λ/D where D is the pupil diameter. The first solution is to correct the wavefront in real time so as to keep the wavefront perturbations smaller than the wavelength. This is achieved with an AO system. The second solution, so-called *speckle interferometry* (Labeyrie 1970), is to take short exposures with respect to the time-scale of the perturbation, and to average the squared modulus of the Fourier transform of the image. This way, the transfer function for the modulus of the Fourier transform of the observed brightness distribution becomes

$$\text{OTF}_k = \sqrt{\left\langle \left| \sum_{(i,j)\in\mathcal{B}_k} G_i\, G_j^\star \right|^2 \right\rangle} \tag{9}$$

and is attenuated for spatial frequencies higher than r_0/λ but different from zero up to D/λ. The Fourier phase of the observed brightness distribution can be retrieved by means of a third-order technique such as the bispectrum (Weigelt 1977).

Here we propose an alternative approach. Instead of averaging the OTF, the goal is to have real-time measurements of the complex amplitude transmission. Then, a post-detection algorithm can be used to obtain a calibrated OTF:

$$\text{OTF}_k = \left\langle \sum_{(i,j)\in\mathcal{B}_k} \frac{G_i\, G_j^\star}{\widetilde{G}_i\, \widetilde{G}_j^\star} \right\rangle, \tag{10}$$

where $\widetilde{G}_i$ and $\widetilde{G}_j$ are estimated complex amplitude transmissions. We have however demonstrated in this section that this information is unavailable on a simple image of the object. In order to recover the missing information, we have proposed a system (Perrin et al. 2006) in which the telescope pupil is injected into an array of single-mode fibres, and rearranged into a new non-redundant exit pupil.

3 FROM AN ILL-POSED TO A WELL-POSED PROBLEM

3.1 The instrument

The concept, proposed in Perrin et al. (2006), is summarized in Fig. 2. Briefly, entrance subapertures collect independently the radiation from an astronomical source in the pupil of the telescope, and focus the light on to the input heads of single-mode optical fibres (of location vectors $\boldsymbol{r}_i$). The radiation is then guided by the fibres down to a recombination unit, in which the beams are rearranged into a 1D or 2D non-redundant configuration to form the exit pupil. Finally, the remapped output pupil is focused to form fringes in the focal plane where a different fringe pattern is obtained for every pair of subpupils.

The amplitudes and phases of the fringes are measurements of the Fourier components given by the entrance baselines vectors $(\boldsymbol{r}_i - \boldsymbol{r}_j)$; the Fourier components measured in the image are thus given by the relation

$$\mu_{i,j} = V_k G_i G_j^\star, \tag{11}$$
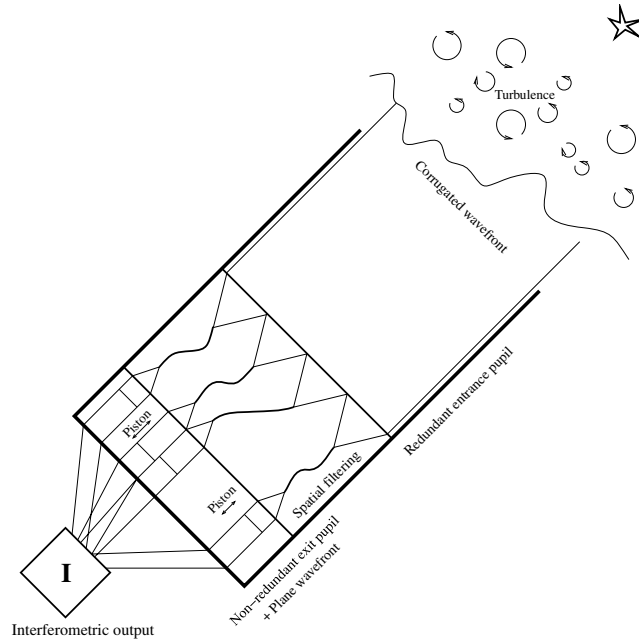
Figure 2. In this instrument, the pupil (or an image of it) is subdivided into several subpupils whose outputs are injected into single-mode fibres. The fibres are then rearranged to create a new non-redundant pupil. Imaging on the detector is then performed as if no remapping had taken place.

where V_k is the complex visibility of the observed object at the frequency $\boldsymbol{u}_k = (\boldsymbol{r}_i - \boldsymbol{r}_j)/\lambda$, and G_i and G_j are the complex transmission factors in the telescope pupil as defined in equation (3). It is interesting to note the differences between this relation and equation (7): thanks to the remapping, each measurement now corresponds to a single pair of subapertures.

A second advantage of this set-up comes from the fact that single-mode fibres act as spatial filters. As a consequence, the relation $G_i = g_i\,e^{i\phi_i}$ is exact for each subpupil. Indeed, after being filtered by the fibre, the complex electric field, which is otherwise a continuous function, can be characterized by only two parameters: its phase and its amplitude. The discretization introduced in the previous section is no longer an approximation which opens the way towards searching for an exact solution.

3.2 On the uniqueness of the solution

The fundamental idea of this paper comes from the fact that by using interferometric techniques, information can be retrieved to deconvolve an image from its PSF. As stated in Section 2, image restoration requires the knowledge of the complex transmission terms G_i, which is impossible with direct imaging. However, Greenaway (1982) proved that the missing information can be encoded at higher frequencies (see also Arnot 1983; Arnot et al. 1985). Remapping enables an increase in the number of observables μ while keeping the number of unknowns constant. This is possible since the complex visibilities V_k only depend on the baselines in the telescope entrance pupil. They do not change with a rearrangement of the pupil (Tallon & Tallon-Bosc 1992).

This can be well understood in terms of unknowns and observables. A remapped system is governed by equation (11). Providing M subapertures and R redundant entrance baselines, the number of complex unknowns are of $M(M-1)/2 - R$ visibilities (V_k terms), and $M-1$ transmission factors (G_i terms). On the other hand, the number of measurements is $M(M-1)/2$ (the $\mu_{i,j}$ terms; with $i \neq j$). Hence, if $R > M-1$, there are more observables than unknowns and the system of equations can be solved.

The fact that both the V_k and the G_i terms can be deduced from the $\mu_{i,j}$ can be illustrated in a specific case. Fig. 3 is the same sketch as in Fig. 1, but with the six subpupils rearranged into a non-redundant configuration. This configuration was chosen to be the most compact, but any other non-redundant configuration could have been used (see e.g. Golay 1971). On the left-hand panel are the complex transmission factors of the remapped pupil. The other panels show the Fourier transform values of, from left- to right-hand side, the PSF, the astronomical object, and the image on the detector. The equation linking the observables $\mu_{i,j}$ to the unknowns G_i and V_k is equation (11). Inversion of the resulting set of equations may be possible since the number of unknowns is larger than the number of measurements. This can be demonstrated by using the logarithm of terms in equation (11), which becomes

$$\ln(|\mu_{i,j}|) = \ln(|V_k|) + \ln(g_i) + \ln(g_j), \tag{12}$$

for the real part, and

$$\Phi(\mu_{i,j}) = \Phi(V_k) + \phi_i - \phi_j, \tag{13}$$
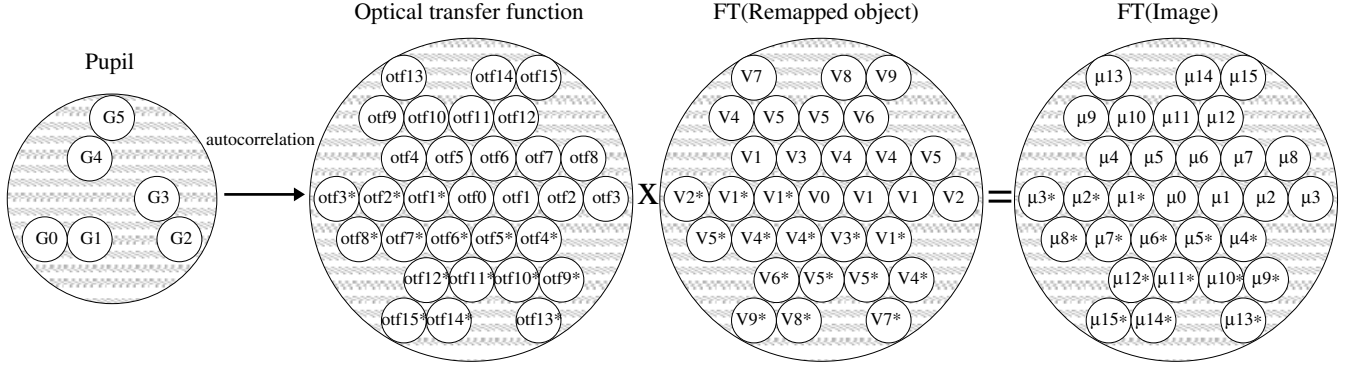
Figure 3. This sketch illustrates equations (4) and (11) in the case of a remapped pupil. As in Fig. 1, the OTF result from the autocorrelation of the pupil complex amplitude transmission, and the Fourier transform of the image is the multiplication of the OTF by the visibility values of the observed object. However, whereas there are still 15 unknown complex values $\{G_0, \ldots, G_5, V_1, \ldots, V_9\}$, the observables provide 15 complex values $\{\mu_1, \ldots, \mu_{15}\}$ and deconvolution is therefore possible.

for the imaginary part. In these two equations, $\Phi()$ is the argument function, and g_i, g_j, ϕ_i and ϕ_j are as defined in equation (3). We obtain this way two sets of linear equations, one for the phases:

$$[\Phi(\mu)] = \mathbf{M}_P \begin{pmatrix} [\phi] \\ [\Phi(V)] \end{pmatrix} \tag{14}$$

and one for the amplitudes:

$$[\ln(|\mu|)] = \mathbf{M}_A \begin{pmatrix} [\ln(g)] \\ [\ln(|V|)] \end{pmatrix}, \tag{15}$$

where [ ] represents column vectors. $\mathbf{M}_P$ and $\mathbf{M}_A$ are two matrices containing 1, 0 and -1 values. Specifically to the example of Fig. 3, equation (14) becomes

$$
\begin{pmatrix} \Phi(\mu_1) \\ \Phi(\mu_2) \\ \Phi(\mu_3) \\ \Phi(\mu_4) \\ \Phi(\mu_5) \\ \Phi(\mu_6) \\ \Phi(\mu_7) \\ \Phi(\mu_8) \\ \Phi(\mu_9) \\ \Phi(\mu_{10}) \\ \Phi(\mu_{11}) \\ \Phi(\mu_{12}) \\ \Phi(\mu_{13}) \\ \Phi(\mu_{14}) \\ \Phi(\mu_{15}) \end{pmatrix}
=
\begin{pmatrix}
1 & -1 & 0 & 0 & 0 & 0 & 1 & 0 & 0 & 0 & 0 & 0 & 0 & 0 & 0 \\
0 & 1 & -1 & 0 & 0 & 0 & 1 & 0 & 0 & 0 & 0 & 0 & 0 & 0 & 0 \\
1 & 0 & -1 & 0 & 0 & 0 & 0 & 1 & 0 & 0 & 0 & 0 & 0 & 0 & 0 \\
0 & 0 & 0 & 1 & -1 & 0 & 1 & 0 & 0 & 0 & 0 & 0 & 0 & 0 & 0 \\
0 & 0 & 1 & -1 & 0 & 0 & 0 & 0 & 1 & 0 & 0 & 0 & 0 & 0 & 0 \\
0 & 0 & 0 & 0 & 1 & -1 & 0 & 0 & 0 & 1 & 0 & 0 & 0 & 0 & 0 \\
0 & 1 & 0 & -1 & 0 & 0 & 0 & 0 & 0 & 1 & 0 & 0 & 0 & 0 & 0 \\
1 & 0 & 0 & -1 & 0 & 0 & 0 & 0 & 0 & 0 & 1 & 0 & 0 & 0 & 0 \\
0 & 0 & 1 & 0 & -1 & 0 & 0 & 0 & 0 & 1 & 0 & 0 & 0 & 0 & 0 \\
0 & 0 & 0 & 1 & 0 & -1 & 0 & 0 & 0 & 0 & 1 & 0 & 0 & 0 & 0 \\
0 & 1 & 0 & 0 & -1 & 0 & 0 & 0 & 0 & 0 & 1 & 0 & 0 & 0 & 0 \\
1 & 0 & 0 & 0 & -1 & 0 & 0 & 0 & 0 & 0 & 0 & 1 & 0 & 0 & 0 \\
0 & 0 & 1 & 0 & 0 & -1 & 0 & 0 & 0 & 0 & 0 & 0 & 1 & 0 & 0 \\
0 & 1 & 0 & 0 & 0 & -1 & 0 & 0 & 0 & 0 & 0 & 0 & 0 & 1 & 0 \\
1 & 0 & 0 & 0 & 0 & -1 & 0 & 0 & 0 & 0 & 0 & 0 & 0 & 0 & 1
\end{pmatrix}
\begin{pmatrix} \phi_0 \\ \phi_1 \\ \phi_2 \\ \phi_3 \\ \phi_4 \\ \phi_5 \\ \Phi(V_1) \\ \Phi(V_2) \\ \Phi(V_3) \\ \Phi(V_4) \\ \Phi(V_5) \\ \Phi(V_6) \\ \Phi(V_7) \\ \Phi(V_8) \\ \Phi(V_9) \end{pmatrix}.
$$

The rank of this matrix is 12, while the number of unknowns is 15. The three terms of degeneracy are one for the absolute phase reference, and two for the tip and tilt. Thus, by providing an arbitrary constraint on these three terms (the absolute phase is arbitrary and the tip and tilt only depend on the location of the image centroid), we can perform a singular value decomposition of the matrix and obtain from the measurements $\mu_{i,j}$ a unique solution for the phase of the perturbations and object visibilities. The same method applies to the logarithm of

the amplitude:

$$
\begin{pmatrix}
\ln(|\mu_1|) \\
\ln(|\mu_2|) \\
\ln(|\mu_3|) \\
\ln(|\mu_4|) \\
\ln(|\mu_5|) \\
\ln(|\mu_6|) \\
\ln(|\mu_7|) \\
\ln(|\mu_8|) \\
\ln(|\mu_9|) \\
\ln(|\mu_{10}|) \\
\ln(|\mu_{11}|) \\
\ln(|\mu_{12}|) \\
\ln(|\mu_{13}|) \\
\ln(|\mu_{14}|) \\
\ln(|\mu_{15}|)
\end{pmatrix}
=
\begin{pmatrix}
1 & 1 & 0 & 0 & 0 & 0 & 1 & 0 & 0 & 0 & 0 & 0 & 0 & 0 & 0 \\
0 & 1 & 1 & 0 & 0 & 0 & 1 & 0 & 0 & 0 & 0 & 0 & 0 & 0 & 0 \\
1 & 0 & 1 & 0 & 0 & 0 & 0 & 1 & 0 & 0 & 0 & 0 & 0 & 0 & 0 \\
0 & 0 & 0 & 1 & 1 & 0 & 1 & 0 & 0 & 0 & 0 & 0 & 0 & 0 & 0 \\
0 & 0 & 1 & 1 & 0 & 0 & 0 & 0 & 1 & 0 & 0 & 0 & 0 & 0 & 0 \\
0 & 0 & 0 & 0 & 1 & 1 & 0 & 0 & 0 & 1 & 0 & 0 & 0 & 0 & 0 \\
0 & 1 & 0 & 1 & 0 & 0 & 0 & 0 & 0 & 1 & 0 & 0 & 0 & 0 & 0 \\
1 & 0 & 0 & 1 & 0 & 0 & 0 & 0 & 0 & 0 & 1 & 0 & 0 & 0 & 0 \\
0 & 0 & 1 & 0 & 1 & 0 & 0 & 0 & 0 & 1 & 0 & 0 & 0 & 0 & 0 \\
0 & 0 & 0 & 1 & 0 & 1 & 0 & 0 & 0 & 0 & 1 & 0 & 0 & 0 & 0 \\
0 & 1 & 0 & 0 & 1 & 0 & 0 & 0 & 0 & 0 & 1 & 0 & 0 & 0 & 0 \\
1 & 0 & 0 & 0 & 1 & 0 & 0 & 0 & 0 & 0 & 0 & 1 & 0 & 0 & 0 \\
0 & 0 & 1 & 0 & 0 & 1 & 0 & 0 & 0 & 0 & 0 & 0 & 1 & 0 & 0 \\
0 & 1 & 0 & 0 & 0 & 1 & 0 & 0 & 0 & 0 & 0 & 0 & 0 & 1 & 0 \\
1 & 0 & 0 & 0 & 0 & 1 & 0 & 0 & 0 & 0 & 0 & 0 & 0 & 0 & 1
\end{pmatrix}
\begin{pmatrix}
\ln(g_0) \\
\ln(g_1) \\
\ln(g_2) \\
\ln(g_3) \\
\ln(g_4) \\
\ln(g_5) \\
\ln(|V_1|) \\
\ln(|V_2|) \\
\ln(|V_3|) \\
\ln(|V_4|) \\
\ln(|V_5|) \\
\ln(|V_6|) \\
\ln(|V_7|) \\
\ln(|V_8|) \\
\ln(|V_9|)
\end{pmatrix}.
$$

The rank of this matrix is 14, meaning all the amplitudes can be retrieved, except for the total brightness of the object. This parameter can easily be constrained by normalizing the flux of the reconstructed image. The measurement of the amplitudes is an important issue since we have to correct for injection variability in the single-mode fibres.

It is however clear that solving this system would require taking the logarithm of the measurements. This would be very sensitive to additive noise. To get the best out of the data, it is better to fit the measurements using their complex values and equation (11). To do so, we developed a self-calibration algorithm which permits the use of thousands of snapshot all together to reconstruct an image up to the photon noise limit.

3.3 A self-calibration algorithm for redundant arrays

This section presents a self-calibration algorithm adapted to single-mode pupil remapping instruments, but also more generally to any kind of redundant interferometric array. Indeed, the equation $\mu_{i,j} = V_k G_i G_j^\star$ established in Section 3.1 is common to all interferometric facilities. In the case of long-baseline interferometry, for example, $\mu_{i,j}$ is the measurement of the complex coherence value between telescopes i and j, G_i the complex transmission factor of telescope i, and V_k the complex visibility of the astronomical object at the baseline formed by telescope i and j.

The particularity of this self-calibration algorithm comes from the fact that it gives complex visibility estimations without the need of a regularization term. This is possible thanks to the redundancy of the interferometric array. If one wants to make sure this algorithm is adapted to a specific interferometric facility, he would have first to establish the $\mathbf{M}_P$ and $\mathbf{M}_A$ matrices, and thus verify the uniqueness of the solution.

In the next sections, we first start deriving an algorithm in the single-exposure case (Sections 3.3.1, 3.3.2 and 3.3.3), and then we show how to extend our algorithm to account for multiple exposures (Sections 3.3.4 and 3.3.5).

3.3.1 Log-likelihood

Following the Goodman (1985) model for the noise of measured complex visibilities, we assume that different measured complex visibilities are uncorrelated and that, for a given measured complex visibility $\mu_{i,j}$, the real and imaginary parts are uncorrelated Gaussian random variables which have the same standard deviation. Under these assumptions and from equation (11), the log-likelihood of the data is

$$
\ell(\mathbf{V}, \mathbf{G}) = \sum_k \sum_{(i,j)\in\mathcal{B}_k} w_{i,j} \, |\mu_{i,j} - G_i G_j^\star V_k|^2, \tag{16}
$$

where G_i and G_j are the complex transmissions for each subaperture and where $\mathcal{B}_k$ is the set of subaperture pairs for which the interferences sample the kth spatial frequency $\boldsymbol{u}_k$ as defined by equation (5). In equation (16), the statistical weights are

$$
w_{i,j} = \frac{1}{\text{Var}(\text{Re}(\mu_{i,j}))} = \frac{1}{\text{Var}(\text{Im}(\mu_{i,j}))}. \tag{17}
$$

Solving the image reconstruction problem, in the maximum likelihood sense, consists of seeking the complex transmissions G_i and the object visibilities V_k which minimize the value of $\ell(V, G)$ given by equation (16). Unfortunately, the log-likelihood $\ell(V, G)$ being a polynomial of sixth degree with respect to the unknowns (the V_k values and the G_i values), proper means to minimize it have to be invented.

3.3.2 Best object visibilities

Given the complex transmissions G, the expression of $\ell(V, G)$ in equation (16) is quadratic with respect to the object complex visibilities V. Providing the complex transmissions G are known, obtaining the best object complex visibilities V is then a simple linear least-squares problem. The solution of this problem is found by solving

$$\frac{\partial \ell}{\partial V_k} = 0, \quad \forall k, \tag{18}$$

where, by linearity, the derivative of the real quantity $\ell(V, G)$ with respect to the complex V_k is defined as

$$\frac{\partial \ell}{\partial V_k} \overset{\text{def}}{=} \frac{\partial \ell}{\partial \mathrm{Re}(V_k)} + \mathrm{i}\, \frac{\partial \ell}{\partial \mathrm{Im}(V_k)}. \tag{19}$$

Then

$$\begin{aligned}
\frac{\partial \ell}{\partial V_k} &= 2 \sum_{(i,j)\in\mathcal{B}_k} w_{i,j}\, \left(G_i\, G_j^\star\, V_k - \mu_{i,j}\right)\, G_i^\star\, G_j \\
&= 2\, V_k \sum_{(i,j)\in\mathcal{B}_k} w_{i,j}\, |G_i|^2\, |G_j|^2 - 2 \sum_{(i,j)\in\mathcal{B}_k} w_{i,j}\, \mu_{i,j}\, G_i^\star\, G_j.
\end{aligned} \tag{20}$$

Solving equation (18) with the partial derivative expression in equation (20) yields the best object visibilities given the data and the complex transmissions:

$$V_k^\dagger = \frac{\displaystyle\sum_{(i,j)\in\mathcal{B}_k} w_{i,j}\, G_i^\star\, G_j\, \mu_{i,j}}{\displaystyle\sum_{(i,j)\in\mathcal{B}_k} w_{i,j}\, |G_i|^2\, |G_j|^2}. \tag{21}$$

Not surprisingly, this solution is a weighted sum of the complex visibilities measured by subaperture pairs which sample the kth spatial frequency. The visibilities obtained by equation (21) are not normalized. Assuming that $V_0^\dagger$ corresponds to the null frequency, the following normalization steps ensure that the sought visibilities are normalized:

$$\alpha = V_0^\dagger$$

$$V_k^\dagger \leftarrow V_k^\dagger/\alpha$$

$$G_j \leftarrow \sqrt{\alpha}\, G_j.$$

It is worth noting that the likelihood remains the same after these re-normalization steps.

3.3.3 Self-calibration stage

Since, given the complex transmission factors, the best object complex visibilities can be uniquely derived, the initial optimization problem of $\ell(V, G)$ can be reduced to a smaller problem which consists of finding the complex transmissions which minimize the partially optimized log-likelihood:

$$\ell^\dagger(G) \overset{\text{def}}{=} \ell(V, G)|_{V=V^\dagger(G)}, \tag{22}$$

where $V^\dagger(G)$ is given by equation (21), possibly after the re-normalization steps. The second stage of our algorithm therefore consists of fitting the complex transmissions so as to minimize $\ell^\dagger(G)$ with respect to the complex transmissions.

Since the criterion $\ell^\dagger(G)$ is continuously differentiable, its partial derivatives cancel at any extremum of the criterion. Hence the so-called *first-order optimality condition* that at the optimum of $\ell^\dagger(G)$ we must have:

$$\frac{\partial \ell^\dagger(G)}{\partial G_i} = 0, \quad \forall i. \tag{23}$$

Note that, unless $\ell^\dagger(G)$ is strictly convex with respect to the G_i values, equation (23) is a necessary condition but is not a sufficient one because it would be verified by all the extrema (local minima, local maxima or saddle points) of the criterion.

Since $V^\dagger$ depends on G, the chain rule must be applied to derive the partial derivative of $\ell^\dagger(G)$ with respect to the ith complex transmission. For instance, the derivative with respect to the real part of the ith complex transmission expands as

$$\begin{aligned}
\frac{\partial \ell^\dagger(G)}{\partial \mathrm{Re}(G_i)} =&\ \frac{\partial \ell(V, G)}{\partial \mathrm{Re}(G_i)}\bigg|_{V=V^\dagger(G)} + \sum_k \frac{\partial \ell(V, G)}{\partial \mathrm{Re}(V_k)}\bigg|_{V=V^\dagger(G)} \frac{\partial \mathrm{Re}\left(V_k^\dagger\right)}{\partial \mathrm{Re}(G_i)} \\
&+ \sum_k \frac{\partial \ell(V, G)}{\partial \mathrm{Im}(V_k)}\bigg|_{V=V^\dagger(G)} \frac{\partial \mathrm{Im}\left(V_k^\dagger\right)}{\partial \mathrm{Re}(G_i)}.
\end{aligned}$$

However, since $V^{\dagger}$ minimizes $\ell(V, G)$, we have

$$\left.\frac{\partial \ell(V, G)}{\partial V_k}\right|_{V=V^{\dagger}(G)} = 0,$$

and from the definition in equation (19) of the partial derivative with respect to a complex variable, we deduce that

$$\left.\frac{\partial \ell(V, G)}{\partial \mathrm{Re}(V_k)}\right|_{V=V^{\dagger}(G)} = 0 \quad \text{and} \quad \left.\frac{\partial \ell(V, G)}{\partial \mathrm{Im}(V_k)}\right|_{V=V^{\dagger}(G)} = 0.$$

It follows that

$$\frac{\partial \ell^{\dagger}(G)}{\partial \mathrm{Re}(G_i)} = \left.\frac{\partial \ell(V, G)}{\partial \mathrm{Re}(G_i)}\right|_{V=V^{\dagger}(G)}.$$

Since the same reasoning can be conducted for the derivative with respect to the imaginary part of the complex transmission and by definition of the derivation of a real quantity with respect to a complex variable given in equation (19), the partial derivative of the partially optimized log-likelihood finally simplifies to

$$\frac{\partial \ell^{\dagger}(G)}{\partial G_i} = \left.\frac{\partial \ell(V, G)}{\partial G_i}\right|_{V=V^{\dagger}(G)}. \tag{24}$$

In words, since $V^{\dagger}(G)$ minimizes $\ell(V, G)$ with respect to V, the partial derivative of $\ell^{\dagger}(G) = \ell(V^{\dagger}, G)$ with respect to G is simply the partial derivative of $\ell(V, G)$ with respect to G into which the V is replaced (after derivation) by $V^{\dagger}(G)$. This property helps to simplify the calculations to come and, more importantly, shows that the global optimum must verify the modified first-order optimality condition:

$$\frac{\partial \ell^{\dagger}(G)}{\partial G_i} = \left.\frac{\partial \ell(V, G)}{\partial G_i}\right|_{V=V^{\dagger}(G)} = 0, \quad \forall i. \tag{25}$$

Finally, the partial derivative of $\ell^{\dagger}$ with respect to the complex transmissions G can be written as

$$\begin{aligned}
\frac{\partial \ell^{\dagger}(G)}{\partial G_i} &= \left.\frac{\partial \ell(V, G)}{\partial G_i}\right|_{V=V^{\dagger}(G)} \\
&= -2 \sum_k \sum_{j:(i,j)\in\mathcal{B}_k} w_{i,j} \left(\mu_{i,j} - G_i G_j^{\star} V_k\right) G_j V_k^{\star} \\
&\quad -2 \sum_k \sum_{j:(j,i)\in\mathcal{B}_k} w_{j,i} \left(\mu_{j,i}^{\star} - G_i G_j^{\star} V_k^{\star}\right) G_j V_k \\
&= 2 G_i \sum_k |V_k|^2 \left[\sum_{j:(i,j)\in\mathcal{B}_k} w_{j,i} |G_j|^2 + \sum_{j:(j,i)\in\mathcal{B}_k} w_{i,j} |G_j|^2\right] \\
&\quad -2 \sum_k \left[\sum_{j:(i,j)\in\mathcal{B}_k} w_{i,j} \mu_{i,j} G_j V_k^{\star} + \sum_{j:(j,i)\in\mathcal{B}_k} w_{j,i} \mu_{j,i}^{\star} G_j V_k\right].
\end{aligned}$$

From this last expression, it is tempting to derive a simple iterative algorithm by solving equation (25) for G_i assuming the other complex transmissions $G_{j:j\neq i}$ are known. The resulting recurrence equation is

$$G_i^{(n+1)} = \frac{\sum_k \left[\sum_{j:(i,j)\in\mathcal{B}_k} w_{i,j} \mu_{i,j} G_j^{(n)} V_k^{(n)\star} + \sum_{j:(j,i)\in\mathcal{B}_k} w_{j,i} \mu_{j,i}^{\star} G_j^{(n)} V_k^{(n)}\right]}{\sum_k \left|V_k^{(n)}\right|^2 \left[\sum_{j:(i,j)\in\mathcal{B}_k} w_{j,i} \left|G_j^{(n)}\right|^2 + \sum_{j:(j,i)\in\mathcal{B}_k} w_{i,j} \left|G_j^{(n)}\right|^2\right]}, \tag{26}$$

where $G_j^{(n)}$ is the jth complex transmission at nth iteration of the algorithm and $V_k^{(n)}$ is the kth best object visibility computed by equation (21) with the complex transmissions estimated at nth iteration:

$$V^{(n)} \stackrel{\text{def}}{=} V^{\dagger}\left(G^{(n)}\right). \tag{27}$$

3.3.4 Multiple exposure case

Our algorithm can be generalized to the processing of multiple exposures of the same object. We assume that the instrument does not undergo any significant rotation with respect to the observed object so that the sampled spatial frequencies (the u_k values) and the corresponding sets of subaperture pairs (the $\mathcal{B}_k$ values) remain the same during the total observing time. We also assume that the object brightness distribution is stable so that the object complex visibilities (the V_k values) do not depend on the exposure time. At least because of the noise and of the

turbulence, the measured complex visibilities and the instantaneous complex amplitude transmissions however do depend on the exposure index t and are, respectively, denoted $\mu_{i,j,t}$ and $G_{i,t}$. Under the Goodman (1985) approximation, the log-likelihood becomes

$$\ell(\boldsymbol{V}, \boldsymbol{G}) = \sum_t \sum_k \sum_{(i,j) \in \mathcal{B}_k} w_{i,j,t} \left| \mu_{i,j,t} - G_{i,t} \, G_{j,t}^\star \, V_k \right|^2, \tag{28}$$

where the, possibly time-dependent, statistical weights are

$$w_{i,j,t} = \frac{1}{\mathrm{Var}(\mathrm{Re}(\mu_{i,j,t}))} = \frac{1}{\mathrm{Var}(\mathrm{Im}(\mu_{i,j,t}))}. \tag{29}$$

Since the object visibilities and the instrumental geometry do not depend on time, the same spatial frequency is measured at every exposure by a given pair of subapertures. Hence the condition given in equation (18) can be used to trivially obtain the best complex visibilities of the object:

$$V_k^\dagger = \frac{\displaystyle\sum_t \sum_{(i,j) \in \mathcal{B}_k} w_{i,j,t} \, G_{i,t}^\star \, G_{j,t} \, \mu_{i,j,t}}{\displaystyle\sum_t \sum_{(i,j) \in \mathcal{B}_k} w_{i,j,t} \, |G_{i,t}|^2 \, |G_{j,t}|^2}, \tag{30}$$

which simplifies to equation (21) in the case of a single exposure.

The updating formula for the time-dependent complex transmissions is obtained from the condition in equation (25) by simply replacing the aperture index i by an aperture–time index i, t and straightforwardly

$$G_{i,t}^{(n+1)} = \frac{\displaystyle\sum_k \left[\displaystyle\sum_{j:(i,j) \in \mathcal{B}_k} w_{i,j,t} \, \mu_{i,j,t} \, G_{j,t}^{(n)} \, V_k^{(n)\star} + \displaystyle\sum_{j:(j,i) \in \mathcal{B}_k} w_{j,i,t} \, \mu_{j,i,t}^\star \, G_{j,t}^{(n)} \, V_k^{(n)} \right]}{\displaystyle\sum_k \left| V_k^{(n)} 1 \right|^2 \left[\displaystyle\sum_{j:(i,j) \in \mathcal{B}_k} w_{j,i,t} \, \left| G_{j,t}^{(n)} \right|^2 + \displaystyle\sum_{j:(j,i) \in \mathcal{B}_k} w_{i,j,t} \, \left| G_{j,t}^{(n)} 1 \right|^2 \right]}, \tag{31}$$

which also simplifies to equation (26) in the case of a single exposure.

3.3.5 Algorithm summary

Putting everything together, our algorithm consists of the following steps:

(i) initialization: set $n = 0$ and choose the starting complex transmissions $\boldsymbol{G}^{(0)}$;

(ii) compute the best object visibilities $\boldsymbol{V}^{(n)}$ given the complex transmissions $\boldsymbol{G}^{(n)}$ according to equation (30) and, optionally, re-normalize the unknowns;

(iii) terminate if the algorithm converged; otherwise, proceed with next step;

(iv) compute $\boldsymbol{G}^{(n+1)}$ by updating the complex transmissions according to equation (31);

(v) let n: $n + 1$ and loop to step (ii).

Our iterative algorithm is very simple to implement and its modest memory requirements makes it possible to process over several thousands of snapshots all together. This is a requirement for faint objects or to achieve very high dynamic range. Yet, on a strict mathematical point of view, our algorithm may have a number of deficiencies. First, as already mentioned, the first-order optimality condition is necessary but not sufficient to ensure that the global minimum (or even a local minimum) of $\ell^\dagger(\boldsymbol{G})$ has been reached. Other non-linear image reconstruction algorithms (blind deconvolution, optical interferometry imaging, etc.) have the same restriction. In practice, checking that the algorithm converges towards a similar solution for different initial conditions can be used to assert the effective robustness of the method. A second possible problem results from the updating of the complex transmission by equation (31). If a fixed point is discovered by the recursion, then it satisfies the necessary optimality condition; but it is also possible that the recursion gives rise to oscillations for the values of the sought parameters. Note that our updating method is a non-linear one, analogous to numerical methods for solving linear equations such as the Jacobi and Gauss–Seidel methods (Barrett et al. 1994). Unlike for our specific problem, it is however possible to prove the convergence of the recursion in the linear case. Again, the behaviour of the algorithm in practice can effectively prove its ability to converge to a fixed point. If it appears that the update formula leads to oscillations, this problem can be completely solved by using an iterative optimization algorithm which guarantees that the partially optimized log-likelihood $\ell^\dagger(\boldsymbol{G})$ is effectively reduced from one iteration to another. Since the log-likelihood is a sum of squares, a Levenberg–Marquardt algorithm (Moré 1977) coupled with a trust region method (Moré & Sorensen 1983) would completely solve this problem. In practice, none of the numerous simulations we have conducted with our iterative algorithm has given rise to any of these convergence problems.

Although derived in the specific case of a pupil remapping instrument, our algorithm shares similarities with the self-calibration method used in radio astronomy (Cornwell & Wilkinson 1981). However, in our case, not only the phases of the complex transmissions are miscalibrated and must be recovered but also the amplitudes. Besides, we do not need a regularization term to overcome the sparsity of the (u, v) coverage by radio interferometers. Our derivation of the non-linear updating formula in equation (31) is also quite similar to the iterative method

proposed by Matson (1991) for recovering the Fourier phase from the bispectrum phase and later improved by Thiébaut (1994) to achieve better convergence capabilities.

4 DYNAMIC RANGE ESTIMATIONS

4.1 Analytical estimation of the photon noise limitations

This system gives calibrated measurements of the spatial frequencies of the object. The advantage is straightforward. In classical imaging, phase and amplitude errors create speckles in the image plane, therefore limiting the dynamic range. With a pupil remapped instrument, and assuming we are acquiring fast enough to *freeze* atmospheric turbulence, statistical errors due to photon and detector noise will theoretically be the main limiting factor. Baldwin & Haniff (2002) showed that the dynamic range of a reconstructed image is linked to the errors of the Fourier components:

$$\text{dyn} = \sqrt{\frac{n}{(\delta V/V)^2 + (\delta\phi)^2}}, \tag{32}$$

where n is the total number of data points, $(\delta V/V)$ is the fractional error in amplitude, and $\delta\phi$ is the phase error (in radians). For a total number of photons N_{ph} and a number of apertures M, the amplitude of the fringe peaks in the Fourier transform of the image is equal to N_{ph}/M (assuming full coherence for the fringes). Considering a white photon noise of amplitude $\sqrt{N_{\text{ph}}}$, the S/N of the visibility modulus can be estimated with

$$V/\delta V = \frac{\sqrt{N_{\text{ph}}}}{M}, \tag{33}$$

as for the phase (Goodman 1985):

$$\delta\phi \approx \frac{\delta V}{V}. \tag{34}$$

This leads to the following approximation of the dynamic range:

$$\text{dyn} = \sqrt{\frac{M(M-1)}{2M^2/N_{\text{ph}}}} \approx \sqrt{\frac{N_{\text{ph}}}{2}}. \tag{35}$$

Within these approximations, this result has the merit of clearly highlighting the advantage and the drawback of a single-mode remapping system: (i) an arbitrarily high dynamic range can be obtained anywhere in the image, providing the integration time is long enough; (ii) since additive noise is uniformly distributed on all the spatial frequencies, it is also evenly distributed across the whole field of view. To compare, an optical design isolating the photons of a bright object next to a faint companion – like a perfect adaptive optics and coronographic system – would achieve a superior photon-wise dynamic range of $\text{dyn} = N_{\text{ph}}$. Extreme dynamic range imaging, as required for detecting extrasolar earths ($\text{dyn} \approx 10^{10}$), would therefore require a longer integration time with our system.

### 4.2 Numerical simulations

4.2.1 Simulation set-up

To perform these simulations, we used YAO, an AO simulation software written by F. Rigaut using the YORICK language. This software allows us to generate corrugated wavefront with and without AO correction. In our simulations, the instrumental set-up corresponds to an 8-m telescope under good seeing condition ($r_0 \approx 20$ cm at 630 nm) caused by four different layers of turbulence at altitudes 0, 400, 6000 and 9000 m. The wind speed ranges from 6 to 20 m s^{-1} depending on the altitude of the layer. The AO system is optimized to work in the near-infrared region. It consists of a classical Shack–Hartmann wavefront sensor and a 12×12 actuator deformable mirror. The loop frequency has been set to 500 Hz, with a gain of 0.6 and a frame delay of 4 ms. The guide star is of magnitude 5.

The remapping was done by dividing the 8-m telescope pupil into 132 hexagonal subpupils of 80 cm in diameter each. They are filtered by the fundamental mode of single-mode fibres, coupled so as to maximize the injection throughput of an uncorrupted incoming wavefront. The injection efficiency in this case would be 78 per cent. However, at the operating wavelength of 630 nm, the diameters of the subpupils are large compared to the Fried parameter ($d/r_0 \approx 4$) and the coupling is expected to be much lower without AO (≈ 5 per cent in these simulations). The 132 subpupils are then rearranged in a non-redundant configuration, to produce a total of 8646 sets of fringes on the detector.

The total integration time was set to 40 s. However, because of the coherence time of the atmosphere, acquisition was done by sequences of short acquisition periods. We used a snapshot time of 4 ms, during which we integrated the effects of phase variations. This was a way to account for fringe blurring due to dynamic piston effects. We also added to our measurements the photon noise as a Gaussian noise of variance the number of photons on each pixel. The number of photons was computed to account for a coupling efficiency of 5 per cent into the fibres and a spectral bandpass of 60 nm.

No chromatic fringe blurring was introduced since its influence would highly depend on the chosen technical set-up. Moreover, there are several ways to avoid this problem. In the case of a 1D non-redundant remapping, we recommend spectrally dispersing the fringes. If a 2D non-redundant reconfiguration is mandatory due to a large number of subpupils, another solution could be to use a hyperchromatic magnifier

Long exposure   Speckle deconvolution   Remapping & deconvolution
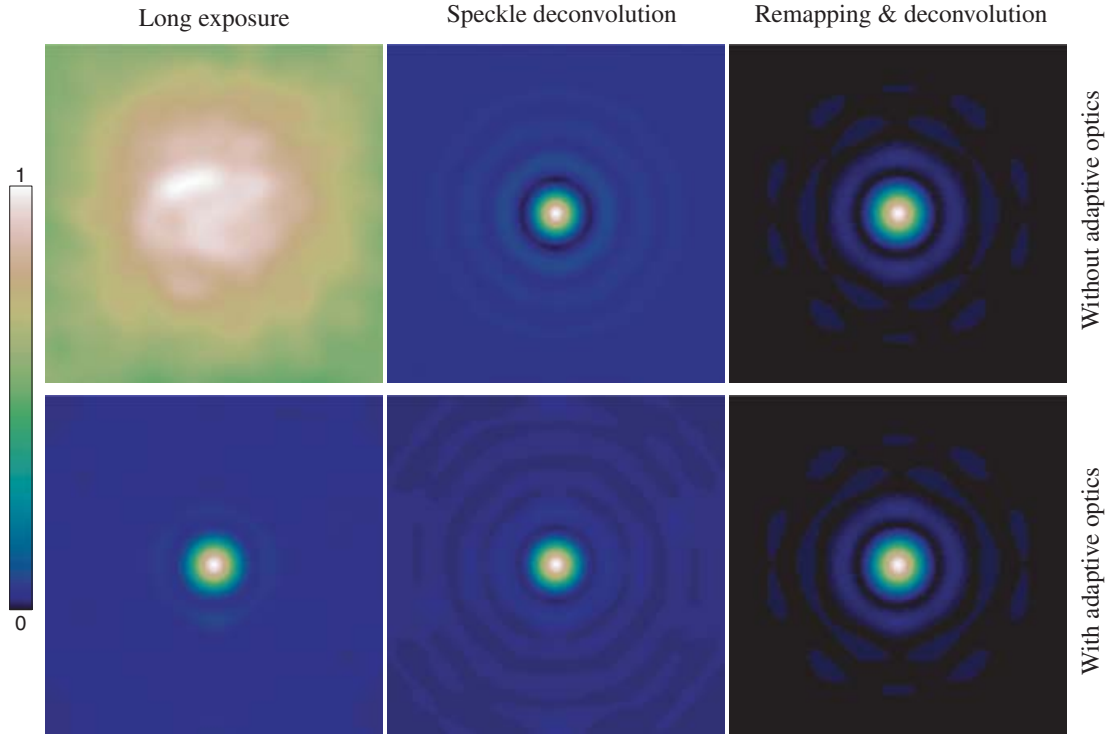
Figure 4. PSFs of the instrument using different imaging techniques. The point-like object is a star of magnitude 5, observed at 630 nm. The acquisition setting consists of 10 000 snapshots of 4 ms each on an 8-m telescope. Left-hand panels: average of the exposures over the total acquisition time (cf. equation 8). Central panels: reconstruction obtained by using conventional speckle interferometry technique (cf. equation 9). Right-hand panels: PSF after remapping and correction by its estimation (cf. equation 10). Upper panels: the PSF is obtained through an atmospheric turbulence of $r_0 \approx 20$ cm ($D/r_0 \approx 40$). Lower panels: PSF with the same corrugated wavefront but corrected by a simulated AO system. The field of view of each image is around 15 resolution elements ($15 \lambda/D$). The PSF quality goes from bad (long exposure without AO), to medium (AO correction and/or speckle deconvolution), to perfect (after a remapping and a post-detection processing).

like a Wynne lens system (as proposed by Ribak, Perrin & Lacour 2004). At least, the use of a narrow spectral filter can completely avoid the chromatic blurring.

4.2.2 Comparison with the speckle and AO techniques

This first test was performed in order to demonstrate the reconstruction quality of the PSF. The astronomical object is a point-like source of Fourier transform values 1 ($V_k = 1$, $\forall k$). The observing wavelength is 630 nm. As described in the previous section, the simulated dataset consists of 10 000 snapshots, each featuring 8646 fringe sets. From each set of fringes, a complex coherence value $\mu_{i,j}$ is extracted, and complex transmission factors $\widetilde{G}_i$ are estimated according to the iterative algorithm described in Section 3.3.3. Finally, we used equation (10) to obtain the calibrated OTF, and thus the PSF. For comparison, the same corrugated wavefronts were used to obtain the PSF with two other techniques. The first one consists of averaging the complex instantaneous OTF by equation (8). The second one (speckle interferometry) consists of averaging the squared modulus, removing photon noise bias and taking the square root as in equation (9). In this work, we did not make use of the bispectrum or closure phase since our object is point-like and therefore purely symmetric. The four left-hand panels of Fig. 4 represent the deduced PSF, with (lower panels) and without (upper panels) the use of an AO system.

The first result confirms the usefulness of both speckle interferometry and AO systems, even though we are observing at visible wavelengths. This is clearly seen in Fig. 5, where unlike uncorrected long exposure imaging, they permit the retrieval of spatial information at the diffraction limit of the telescope. Nevertheless, the Strehl ratio in images obtained by these techniques is very low and the background pollution remains important. Without remapping, the best dynamic range achievable at visible wavelength is with a combination of AO and speckle interferometry technique, which provide a dynamic range of 40. This of course is in the case of a perfectly working near-infrared AO system with a 500 Hz frequency loop. Most current AO systems are not used in that mode since any slight miscalibration of the actuator influence function would make it useless at these wavelengths.

On the other hand, a diffraction pattern is obtained by using our remapping instrument and our image reconstruction algorithm. The pattern differs slightly from a perfect Airy disc due to the hexagonal sampling of the OTF. At a few λ/D from the central star, a dynamic range of 10^3 is obtained (see Fig. 5). Using an AO system does not significantly modify the pattern, meaning that the dynamic range is limited by the shape of the perturbation free PSF. Our conclusion is therefore that the dynamic range could be further increased by choosing a different PSF. We did this in the following section over a complex astronomical object.
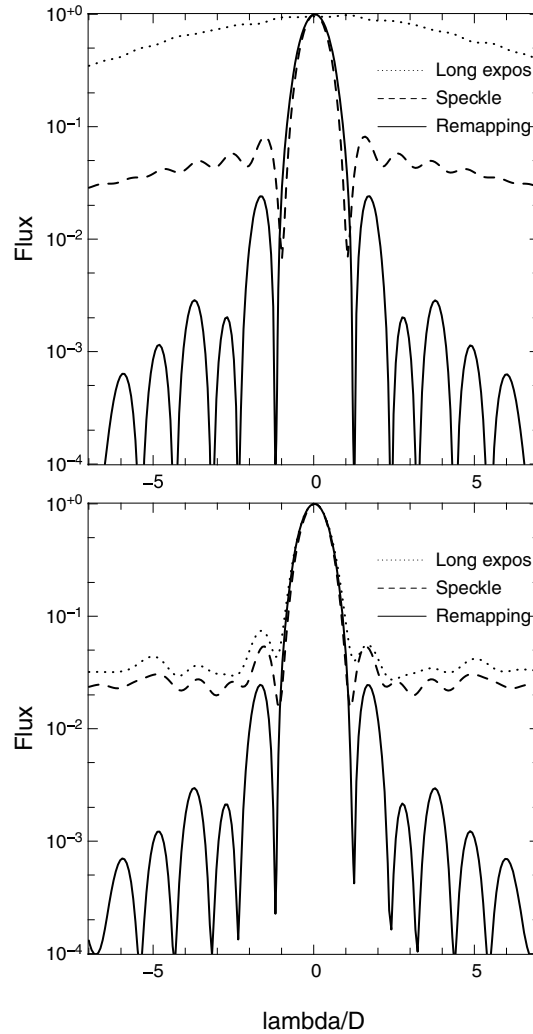
Figure 5. Horizontal cuts of the PSFs imaged in Fig. 4. The source is a star of magnitude 5, observed at 630 nm. The acquisition setting consists of 10 000 snapshots of 4 ms each on an 8-m telescope ($r_0 \approx 20$ cm). The upper panel shows the PSF after an uncorrected turbulence, while the lower panel shows the PSF after partial correction of the wavefront by an AO system. The three curves are obtained through the equations (8)–(10). The last equation requires a pupil remapping to get an estimation of the $\widetilde{G}_i$ and $\widetilde{G}_j$ terms. At a few resolution elements from the star, AO systems and speckle techniques cannot achieve a dynamic range over 40. However, pupil remapping enables a perfect reconstruction of the PSF, with dynamic ranges over 10^3.

4.2.3 Image reconstruction

In this simulation, the astronomical object is a star surrounded by a protoplanetary disc. The disc has an exponential brightness distribution and a total flux of a hundredth of the star flux. Two companions are also present, one with a flux of a thousandth, and the other of ten thousandths the flux of the star.

As before, the G_i complex transmissions are estimated by using iteratively equation (26). But unlike in Section 4.2.2, calibrated object visibilities are retrieved by our algorithm using equation (30) from 10 000 short exposure images. We used these visibilities to reconstruct an image. But instead of doing a simple Fourier transform to obtain the equivalent of a *dirty map*, it is possible to choose the PSF according to a scientific goal. For example, an Airy disc PSF is good to achieve high angular resolution, while a Gaussian apodization is better for the dynamic range. Of course, any other visibility apodization can also be applied to obtain the most suitable PSF. This system thus has the advantage of producing images close to what can be obtained with optically apodized pupil optics (Kuchner & Traub 2002; Guyon 2003), while completely free of any atmospheric perturbations. This way, the dynamic range is no longer limited by the Airy rings of the diffraction pattern of the telescope.

However, there is one perturbation this system cannot correct for: it is the photon noise. The phase corrugation being accounted for, the photon noise should be the theoretical limit of the dynamic range. To try to reach this limit, we used a Gaussian shape apodization on the visibilities. All of the image reconstructions in Fig. 6 are of the object described in the first paragraph of this section, but with different total brightnesses. The reconstructions from the left- to right-hand panels are, respectively, of a central star of magnitude 15, 10, 5 and 0. The upper set of panels are for a system without AO, while the four bottom panels are with AO activated. Fig. 7 gives a summary by plotting a

Star Magnitude = 15   10   5   0
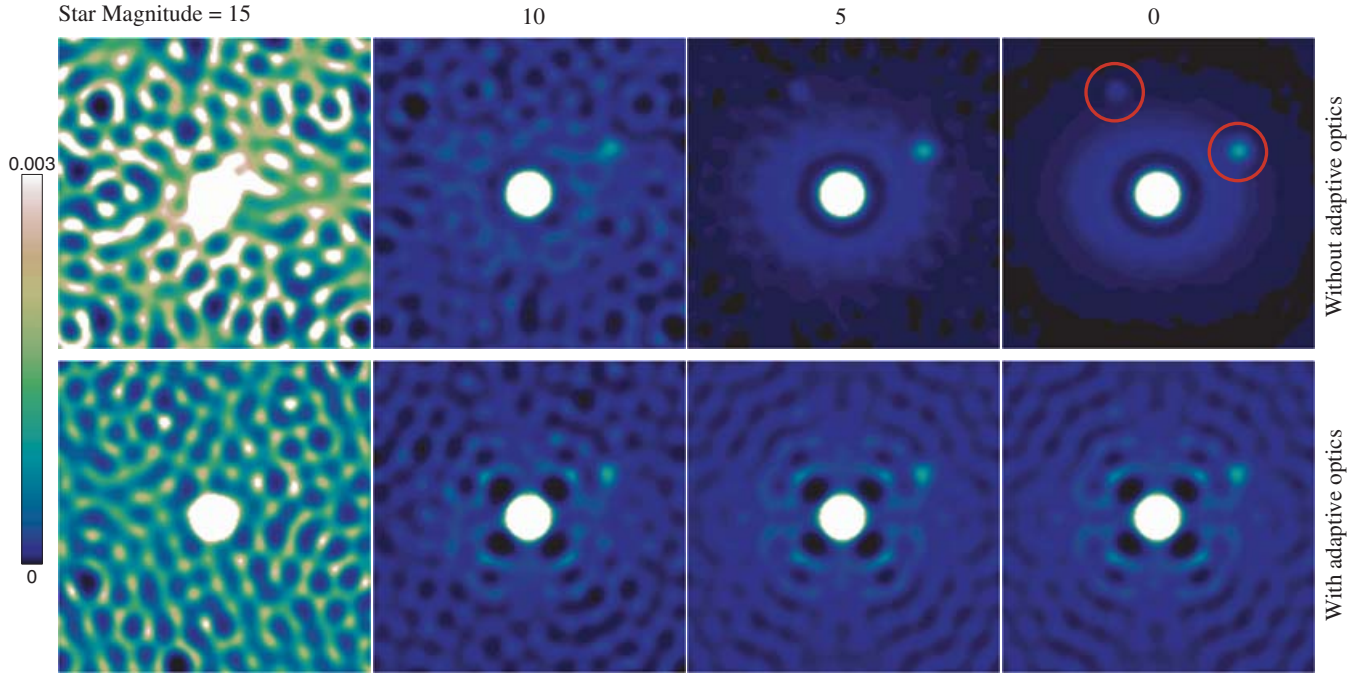
Figure 6. These simulations feature reconstructed images from the visibilities acquired from equation (21). The acquisition settings consist of 10 000 snapshots of 4 ms each on an 8-m telescope in the visible ($r_0 \approx 20$ cm). The object is a central star with a protoplanetary disc and two companions, of relative flux a thousandth and ten thousandths (respectively, at the upper right and upper left of the central star – they are highlighted by the red circles on the upper right-hand image). From left- to right-hand panels, the differences in the reconstructed images are due to the brightness of the object (magnitudes 15, 10, 5 and 0). The upper panels are reconstructed images in the case of an uncorrected wavefront ($D/r_0 \approx 40$). The lower panels are reconstructed images with an AO corrected wavefront. The field of view of each image is around 30 resolution elements (30 λ/D). The colour scale of the panels is linear, from 0 to 3×10^{-3}, and normalized to the flux of the central star. The reconstructions show dynamic range around or over 10^4, except for the ones with a star of magnitude 15. In the three upper panels, we can clearly see the photon noise limit, evolving as a function of the brightness of the source. For faint sources, the lower right-hand panel shows that dynamic range is increased by combining a remapping set-up with an AO system. However, on a bright source, fringe smearing due to the high-frequency control loop of the deformable mirror limits the dynamic range. An horizontal cut of these figures can be seen in Fig. 7.

Table 1. Dynamic range results.

| | Without AO | | With AO | |
Magnitude	$\sqrt{N_{\mathrm{ph}}/2}$ [a]	DR[b]	$\sqrt{N_{\mathrm{ph}}/2}$ [a]	DR[b]
0	1.1×10^6	0.9×10^6	2.4×10^6	1.8×10^4
5	1.1×10^5	1.5×10^5	2.4×10^5	1.7×10^4
10	1.1×10^4	1.3×10^4	2.4×10^4	1.6×10^4
15	1.1×10^3	0.8×10^3	2.4×10^3	1.2×10^3

[a]Theoretical dynamic range as predicted by equation (35).
[b]Dynamic range obtained by taking the background rms of the reconstructed images of Fig. 6.

horizontal cut of the different reconstructions. Table 1 lists the dynamic ranges estimated on the images and compares them with the analytical approximation of the photon noise established in Section 4.1. The dynamic range estimations are obtained by taking the inverse of the rms of the background of the image normalized by its pixel of maximum flux.

When atmospheric turbulence is not corrected by an AO system, the reconstructions clearly highlight a dynamic range limited by photon noise. For an object of magnitude 10, we achieved a dynamic range of 1.3×10^4. This is comparable to what was calculated from the total photon count and the analytical relation dyn $\approx \sqrt{N_{\mathrm{ph}}/2}$. This theoretical value, taking into account the 5 per cent coupling efficiency in the fibres, was 1.1×10^4. A second interesting point is that when the brightness of the source increases by a factor of 100 (delta mag = 5), the dynamic range increases by a factor of around 10. This can be seen over 15 orders of magnitude, indicating that the dynamic range has a roughly linear increase as a function of $\sqrt{N_{\mathrm{ph}}}$. This does (1) confirm the validity of the analytical estimation and (2) prove the quality of our self-calibration algorithm to restore the object visibilities.

Noteworthy is the reconstruction of the system with a brightness of 15 mag. Due to a relatively low coupling efficiency in the fibres, an average of 250 photons are detected per 4-ms snapshot. According to equation (33), it implies an S/N of ≈ 0.12 for each spatial frequency measurement. It is therefore impressive to note that even with such a vague knowledge of the $\mu_{i,j}$, the iterative algorithm of Section 3.3.3 is
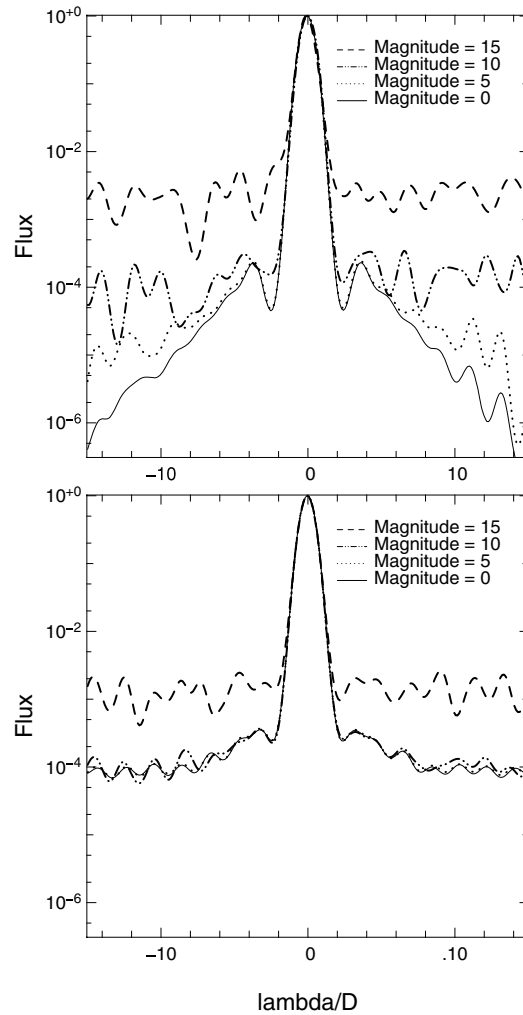
Figure 7. Horizontal cuts of the reconstructed images shown in Fig. 6. The acquisition setting consists of 10 000 snapshots of 4 ms each on an 8-m telescope ($r_0 \approx 20$ cm). The upper panel shows the reconstruction in the case of an uncorrected turbulence, while the lower panel shows the reconstruction with AO correction. On the upper panel, we can clearly see the dynamic range improving with the brightness of the source, from 10^3 (15 mag), to 10^6 (0 mag). At the highest dynamic range, we can see the exponential brightness decrease of the protoplanetary disc. Behind an adaptive optic, deconvolution is no longer limited by the photon noise, but by the high-frequency differential piston introduced by the deformable mirror.

capable of restoring images with a dynamic range limited by the photon noise. This is possible since it combines the advantage of fitting the information from all snapshots together with a small, CPU friendly, recursive algorithm.

When atmospheric turbulence is corrected by an AO system, the dynamic range does not increase linearly as a function of the brightness anymore. Indeed, in the lower panels of Figs 6 and 7, the dynamic range is clearly limited by another factor. Thanks to the correction, the injection throughput is higher, around 23 per cent. This allows an increase in dynamic range for the faintest source, but with a saturation around a few $\times 10^4$. The reason for this unpredicted threshold appeared clearly when analysing our simulations. During the 4 ms integration time, mirror displacements happened twice to adapt for the atmospheric turbulence. These minor corrections, while increasing the spatial coherence (Cagigal & Canales 2000), have the drawback of introducing a phase noise overshoot at the frequency of the loop. This side effect results in a slight blurring of the fringes recorded on the detector and a bias on the measurements. To profit from the advantages of the AO, solutions could be either to increase the acquisition rate, or, better, to adjust the control loop to decrease the amplitude of the overshoot.

5 SUMMARY

In this paper, we presented further investigation of the instrument introduced in Perrin et al. (2006).

(i) We established an analytical relation linking the Fourier components of the image, the Fourier components of the object and the atmospheric perturbations (equation 11). We showed that inverting this equation allowed us to completely disentangle turbulence from astronomical information (Section 3.2).

(ii) We developed an analytical iterative self-calibration algorithm which enables inversion of the previously established equation over several thousands of snapshots simultaneously. This algorithm happened to be robust, allowing visibility determination from Fourier component measurements with S/N well below 1 (Section 3.3).

(iii) Simulations of this system confirmed the validity of the algorithm and produced high dynamic range, diffraction limited, images of complex astronomical objects. A dynamic range of the order of 10^6 was achieved at visible wavelength on an 8-m telescope and in the presence of good seeing conditions. Compared to actual AO systems, it represents an increase of around 10^4 in dynamic range. We noted that the sensitivity of the instrument would increase by using an AO system, but at the price of a limitation in the achievable dynamic range (Section 4).

REFERENCES

Arnot N. R., 1983, Opt. Commun., 45, 380
Arnot N. R., Atherton P. D., Greenaway A. H., Noordam J. E., 1985, Traitement du Signal, 2, 129
Baldwin J. E., Haniff C. A., 2002, Phil. Trans. R. Soc. London, 360, 969
Barrett R. et al., 1994, Templates for the Solution of Linear Systems: Building Blocks for Iterative Methods. SIAM, Philadelphia, PA
Cagigal M. P., Canales V. F., 2000, Opt. Soc. Am. J. A, 17, 903
Cornwell T. J., Wilkinson P. N., 1981, MNRAS, 196, 1067
Golay M. J. E., 1971, J. Opt. Soc. Am., 61, 272
Goodman J. W., 1985, Statistical Optics. Wiley, New York
Greenaway A. H., 1982, Opt. Commun., 42, 157
Guyon O., 2003, A&A, 404, 379
Haniff C. A., Mackay C. D., Titterington D. J., Sivia D., Baldwin J. E., 1987, Nat, 328, 694
Kuchner M. J., Traub W. A., 2002, ApJ, 570, 900
Labeyrie A., 1970, A&A, 6, 85
Matson C. L., 1991, J. Opt. Soc. Am. A, 8, 1905
Moré J. J., 1977, in Watson G. A., ed., Lecture Notes in Mathematics Vol. 630, Numerical Analysis. Springer-Verlag, Berlin
Moré J. J., Sorensen D. C., 1983, SIAM J. Sci. Stat. Comp., 4, 553
Perrin G., Lacour S., Woillez J., Thiébaut E., 2006, MNRAS, 373, 747
Ribak E. N., Perrin G. S., Lacour S., 2004, in Traub W. A., ed., Proc. SPIE Vol. 5491, New Frontiers in Stellar Interferometry. The International Society for Optical Engineering, Bellingham, WA, p. 1624
Tallon M., Tallon-Bosc I., 1992, A&A, 253, 641
Thiébaut E., 1994, PhD thesis, Université de Paris 7
Thiébaut E., 2005, in Foy R., Foy F.-C., eds, NATO ASI, Optics in Astrophysics. Kluwer, Dordrecht
Thiébaut E., Conan J.-M., 1995, J. Opt. Soc. Am. A, 12, 485
Tuthill P. G., Monnier J. D., Danchi W. C., Wishnow E. H., Haniff C. A., 2000, PASP, 112, 555
Weigelt G., 1977, Opt. Commun., 21, 55

This paper has been typeset from a TEX/LATEX file prepared by the author.